

# JGR Solid Earth

## RESEARCH ARTICLE

10.1029/2021JB022152

### Key Points:

- The Southwest Indian Ridge at 50°28'E experienced a high eruption rate and low tectonic strain over the past 780 kyr, despite ultraslow spreading rate
- Seafloor and lava morphologies indicate two successive cycles of waxing and waning magmatic phases, each lasting 300 kyr
- Upper-crustal construction at slow and ultraslow mid-ocean ridges are controlled by melt supply more than spreading rate

### Supporting Information:

Supporting Information may be found in the online version of this article.

### Correspondence to:





J. Chen and C. Tao,  
[chenjie@ipgp.fr](mailto:chenjie@ipgp.fr);  
[taochunhuimail@163.com](mailto:taochunhuimail@163.com)

### Citation:

Chen, J., Cannat, M., Tao, C., Sauter, D., & Munsch, M. (2021). 780 thousand years of upper-crustal construction at a melt-rich segment of the ultraslow spreading Southwest Indian Ridge 50°28'E. *Journal of Geophysical Research: Solid Earth*, 126, e2021JB022152. <https://doi.org/10.1029/2021JB022152>

Received 2 APR 2021  
Accepted 8 AUG 2021

## 780 Thousand Years of Upper-Crustal Construction at a Melt-Rich Segment of the Ultraslow Spreading Southwest Indian Ridge 50°28'E

Jie Chen<sup>1</sup> , Mathilde Cannat<sup>1</sup> , Chunhui Tao<sup>2</sup> , Daniel Sauter<sup>3</sup> , and Marc Munsch<sup>3</sup> 

<sup>1</sup>Institut de physique du globe de Paris, Université de Paris, CNRS, Paris, France, <sup>2</sup>Key Laboratory of Submarine Geosciences, Second Institute of Oceanography, MNR, Hangzhou, China, <sup>3</sup>Institut de Physique du Globe de Strasbourg, UMR—CNRS, Université de Strasbourg, Strasbourg, France

**Abstract** Melt supply at the ultraslow-spreading Southwest Indian Ridge (SWIR) has been shown to vary from nearly amagmatic, leading to ultramafic seafloor, to magmatically robust, producing fully volcanic seafloor. The center of the SWIR 50°28'E segment represents a magmatically robust endmember. High-resolution bathymetry and backscatter, near-bottom magnetic data, and visual observations were acquired to infer spatiotemporal variations in upper-crustal construction over the past 780 kyr. Tectonic strain inferred from observed faults represents <8% of the total plate divergence during this period. Mapped seafloor and lava morphologies show a prevalence of smooth seafloor and smooth hummocky seafloor (64% mapped area), corresponding to a dominance of high-effusion-rate, sheet-lobate lavas, over hummocky seafloor (29%) that mostly comprises low-effusion-rate pillow lavas. This prevalence is most pronounced within a ~5 km-long domain at the segment center, while hummocky seafloor prevails to its east and west, indicating a substantial along-axis decrease in average eruption rate. Across-axis changes of seafloor morphologies and faulting pattern indicate two successive cycles of upper-crustal construction. These cycles last ~300 kyr, interpreted as waxing and waning magmatic phases. During waxing phases, shallow axial melt lenses (AMLs) form beneath the segment center, feeding narrow diking systems that build high-eruption-rate smooth domal volcanos. During waning phases, lower frequencies of melt replenishment may cause the AML to become deeper and ultimately disappear. This configuration triggers diking and hummocky-dominated eruptions over a wider axial domain, with more faults. We propose that modes of upper-crustal construction at slow and ultraslow mid-ocean ridges are influenced by melt supply more than spreading rate.

**Plain Language Summary** The ultraslow-spreading Southwest Indian Ridge (SWIR) is characterized by extremely variable melt supply. Previous studies show that the center of the SWIR 50°28'E segment has a high melt supply with a uniquely 9.5 km-thick crust and a crustal melt-mush zone. Seafloor and lava morphologies, fault scarps and fissures, and eruptive units over the past 780 kyr, were mapped in this high melt supply region, using 2-m resolution bathymetry and backscatter data collected by an autonomous underwater vehicle and seafloor photographs collected by a towed camera. Our geological mapping suggests high eruption rates and low tectonic strain, similar to intermediate- and fast-spreading ridges. It also indicates that the upper crust was constructed with alternating waxing and waning magmatic phases over cycles of ~300 kyr duration. Waxing phases are characterized by high-eruption-rate smooth domal volcanos fed by localized dikes. Based on available geophysical data, waxing phases occur with relatively shallow and frequently replenished axial melt lenses. By contrast, waning phases are dominated by low-eruption-rate hummocky ridges fed by delocalized dikes, corresponding to deeper and shorter-lived axial melt lenses and lower frequency of melt replenishment. We propose that the upper-crustal geology at slow-ultraslow ridges is controlled by melt supply more than spreading rate.

## 1. Introduction

Mid-Ocean Ridges (MORs) are one of the Earth's principal volcanic systems: Magma forms in the upwelling mantle in response to plate divergence, and dike intrusions and volcanic eruptions build the upper crust. Modes of upper-crustal construction have been shown to vary as functions of spreading rate, magma supply, and tectonic deformation (Cannat et al., 2019; Colman et al., 2012; Perfit & Chadwick, 1998). At those ridge

segments that have a crustal magma mush zone capped by a shallow axial melt lens (AML), for example, 9°30'N of fast spreading East Pacific Rise (EPR), as inferred from the detection of a seismic low-velocity anomaly (LVA; Dunn et al., 2000) and an AML reflector (Detrick et al., 1987), volcanic eruptions mostly produce high-eruption-rate, sheet-lobate dominated, smooth lava flows (Fundis et al., 2010). When the AML reflector gets deeper, for example, 91–95°W of intermediate spreading Galapagos Spreading Center (GSC; Blacic et al., 2004), low-eruption-rate hummocky lava flows (pillow dominated) also occur, and meanwhile faults contribute to a larger part of plate divergence (Colman et al., 2012). Key characteristics of the ridge's magma plumbing system possibly can therefore be indirectly inferred from seafloor and lava morphologies, if bathymetry and backscatter data are available at sufficient resolution, and backed by seafloor videos or photographs (Colman et al., 2012; Escartín et al., 2014; Fundis et al., 2010; Sauter et al., 2002; Searle et al., 2010).

Shallow AMLs typically characterize fast spreading ridges, while intermediate spreading ridges tend to have deeper AMLs (Chen & Morgan, 1990). Crustal LVA and/or AML reflectors have not been found as frequently at slow and ultraslow spreading ridges (Detrick et al., 1990; Hooft et al., 2000; Minshull et al., 2006), and hummocky lava flows dominate (Sauter et al., 2002; Searle et al., 2010). However, crustal LVAs and/or AML reflectors that extend only a few kilometers from their segment centers have been documented at a few magmatically robust slow spreading segments, such as the Lucky Strike segment at the Mid Atlantic Ridge (MAR; Combier et al., 2015; Seher et al., 2010; Singh et al., 2006) and the 50°28'E segment at the ultraslow spreading Southwest Indian Ridge (SWIR; Jian, Chen, et al., 2017; Jian, Singh, et al., 2017). These segments display large along-axis variations in both seismic velocity structure and seafloor morphology. Lucky Strike has a dome-shaped volcanic construct built by smooth lava flows above the documented AML at the segment center while ridge-parallel hummocky ridges form toward segment ends (Escartín et al., 2014). This characteristic is consistent with a strong focusing of melt supply on the segment center (Lin et al., 1990). Escartín et al. (2014) listed 16 examples of dome-shaped volcanos at the center of slow and ultraslow spreading ridge segments, and suggested that a crustal melt mush zone is likely to be the key to form such large volcanic constructions and that their common fate is to become rifted by axial graben faults.

Seismic tomography results obtained at the center of the SWIR 50°28'E segment (segment #27 in Cannat et al., 1999; Figure 1a) show a uniquely thick crust (9.5 km) and a rounded crustal LVA ~4–9 km below the seafloor (bsf) with a horizontal diameter of 5–6 km at the –0.4 km/s contour (Jian, Chen, et al., 2017; Jian, Singh, et al., 2017). Seismic reflection data are not available to confirm the existence of an AML on top of this LVA. However, full waveform inversion results show a sharp decrease in seismic velocity at a depth of about 4 km, which is interpreted to be due to mostly crystallized gabbros with up to 10% melt (Jian et al., 2017a). The depth to the Moho indicates that crustal thickness is reduced to 6.6–7.6 km midway to the segment ends (profile B-B' of Jian, Chen, et al., 2017 located in Figure 1a). Seismicity is low beneath the SWIR 50°28'E segment, yet a few microearthquakes have been located down to ~10 km bsf on or close to the ridge axis and at least 3 km laterally to the west of the LVA (Yu et al., 2018), indicating that the brittle lithosphere there is a bit thicker than the crust. The axial domain is bounded by two elevated regions that extend over the full length of the present-day ridge segment (prominent scarps near magnetic anomaly 2A in Figure 1a), and are interpreted by Mendel et al. (2003) as the conjugate rifted remnants of a yet more magmatically robust period of spreading. This period of very high melt influx has been interpreted as due to the eastward migration of a mantle melting anomaly (Sauter et al., 2009). Present-day magmatism at the 50°28'E segment is a bit weaker, even at the segment center (Mendel et al., 2003), but remains more magmatically robust than at other SWIR segments.

Here, we report on high-resolution (HR) bathymetry and backscatter, seafloor videos and photographs, and near-bottom magnetic data, collected over a 13 by 12 km area at the center of the SWIR 50°28'E segment (Figure 1). This survey is located above the LVA and is bounded by the Brunhes-Matuyama (B-M) reversal (780 kyr). It includes the Duanqiao extinct black-smoker hydrothermal field (HF; Tao et al., 2012) and several hydrothermal plume anomalies (Yue et al., 2019). The variations of seafloor and lava flow morphologies at the center of the SWIR 50°28'E segment over the past 780 kyr provide constraints in space and time to improve the general understanding of the effects of spreading rate and melt supply on upper-crustal construction at MORs.

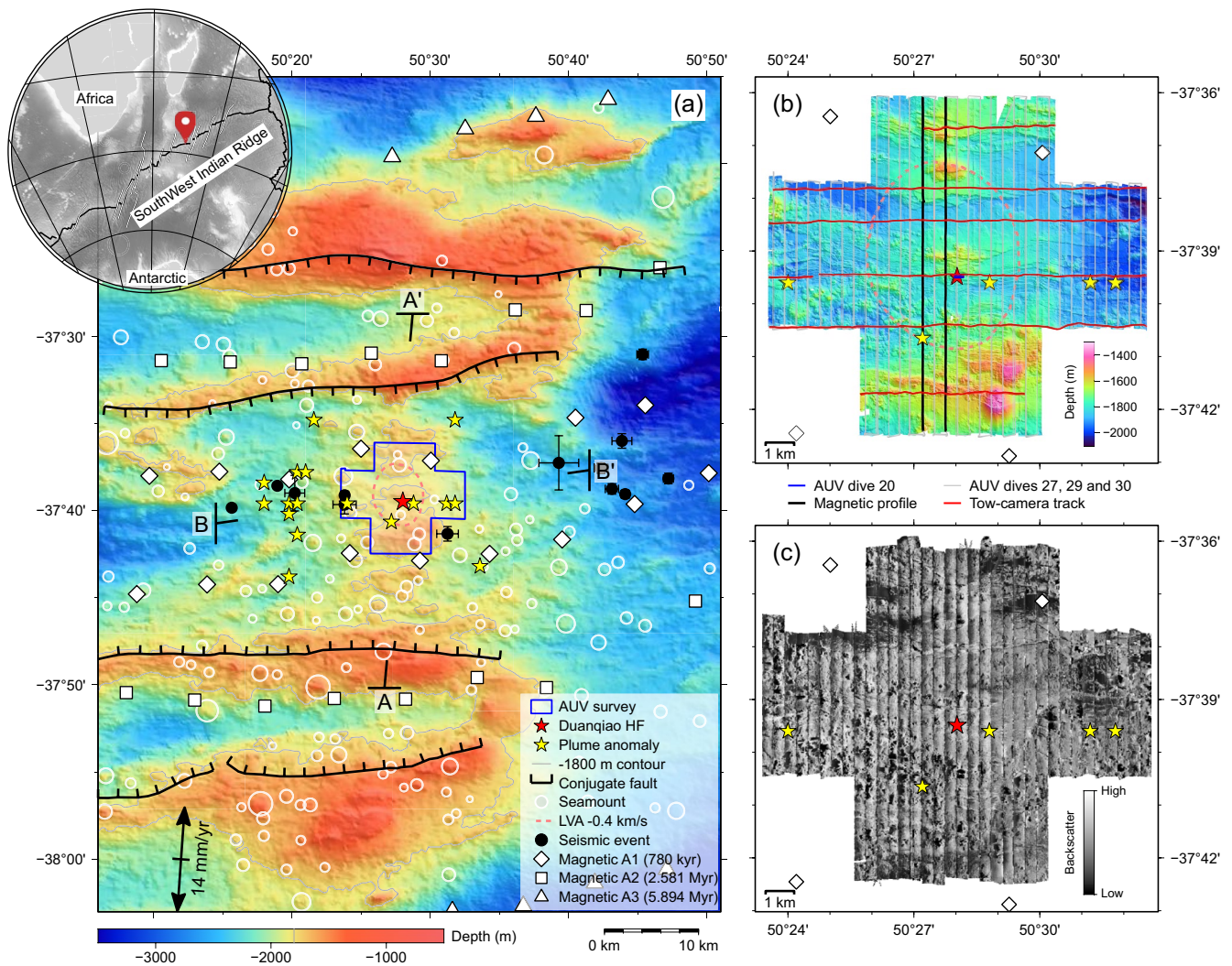


**Figure 1.** (a) Shipboard bathymetric map of 50°28'E segment (segment #27 in Cannat et al., 1999) at the Southwest Indian Ridge (SWIR). Conjugated faults mark the rifted remnants of elevated seafloor regions. Red star is the location of the Duanqiao hydrothermal field, and yellow stars indicate hydrothermal plume anomalies (Yue et al., 2019). Magnetic A1 (Brunhes-Matuyama reversal), A2, and A3 (white-filled symbols) are pickings from sea-surface magnetic anomaly (Sauter et al., 2009). The dashed pink line in panels (a) and (b) outlines the *P*-wave low-velocity anomaly of  $-0.4$  km/s at 7 km bsf, which is calculated by subtracting an average velocity-depth profile within along-axis distance of  $\pm 15$  km (Jian, Chen, et al., 2017). AA' and BB' mark locations of seismic profiles across and along the ridge axis from Jian, Chen, et al. (2017). Black dots with error bars indicate the epicenters of microearthquakes (Yu et al., 2018). (b) and (c) High-resolution (gridded at 2 m) bathymetry and backscatter at the center of 50°28'E segment. Gray lines are tracks of autonomous underwater vehicle (AUV) QianLong-II dives 27, 29, and 30. Thick black lines are two magnetic profiles shown in Figure 7. Red lines show the deep-tow camera tracks. Short blue line near the Duanqiao hydrothermal field is a camera track during AUV dive 20.

## 2. Data and Methods

### 2.1. AUV Surveys

The autonomous underwater vehicle (AUV) QianLong-II investigated the center of the SWIR 50°28'E segment during the DY40 cruise aboard R/V Xiangyanghong-10 in 2016. The AUV was equipped with a newly developed High-Resolution Bathymetric Sidescan Sonar System (HRBSSS; Liu et al., 2016) and a three-component magnetometer (Wu et al., 2019). During dives 27, 29, and 30, the AUV surveyed at an altitude of  $\sim 100$  m above the seafloor at a speed of 1–2 kt with a track spacing of 400 m (Figure 1b). A short AUV-borne camera survey (dive 20) was conducted at  $\sim 5$  m above the seafloor near the Duanqiao HF. Navigation was achieved by combining the inertial navigation system (IXBLUE PHINS-6000) with a long baseline system (Wu et al., 2019).



### 2.1.1. High-Resolution Bathymetry and Backscatter Data

The HRBSSS was operated at 150 kHz with a swath width of 250 m during dives 27, 29, and 30. The bathymetry and backscatter data were processed using the CleanSweep software to create a 2-m resolution grid (Figures 1b and 1c). The combined bathymetry data cover ~110 km<sup>2</sup> of seafloor (13 km along axis and 12 km across axis). The data remain noisy despite processing (the DY40 cruise was the first deep sea operation for the HRBSSS system of the AUV). We were cautious to adapt the scale and scope of our observations to the relatively poor quality of the data.

### 2.1.2. Magnetic Anomalies

For this study, we processed two across-axis magnetic profiles in the center of the AUV map, collected with a 1 Hz sampling frequency (Figure 1b). The magnetic effect from the AUV was estimated and removed (Wu et al., 2019). The local geomagnetic field predicted by International Geomagnetic Reference Field (IGRF) was removed (Thébault et al., 2015), and Reduction-To-Pole (RTP) was applied to locate the anomalies directly above their possible sources by correcting the inclination and declination of the geomagnetic field.

## 2.2. Deep-Tow Video and Seafloor Photographs

In this study, we analyzed 24 h of video and 3,647 photographs covering 6 ridge-parallel transects within the AUV survey area (Figure 1b). These data were collected in 2015 during the DY34 cruise aboard R/V Dayangyihao (Yue et al., 2019) with the Deep-tow Hydrothermal Detection System, navigated with an ultra-short-baseline (USBL) system (Yue et al., 2019).

## 2.3. Geomorphological Analysis

Following previously published geomorphological studies of the MORs (Colman et al., 2012; Escartin et al., 2014; Fundis et al., 2010; Sauter et al., 2002; Searle et al., 2010), we used HR bathymetry and backscatter data to classify distinct seafloor morphologies and to map fault scarps and fissures (Figure 2). Optical seafloor imagery was used to identify lava morphologies, with the occurrence of pillow, lobate, and sheet lavas that have been interpreted as mainly resulting from low, intermediate, and high effusion rates, respectively (Colman et al., 2012; Fundis et al., 2010; Gregg & Fink, 1995). We also tentatively identified eruptive units, which we infer formed during a given eruptive sequence, characterized by similar eruptive dynamics (e.g., Colman et al., 2012), based on seafloor morphology and the nature of their contacts with the surrounding seafloor.

### 2.3.1. Seafloor Morphology Classification

Four distinct seafloor morphologies, that is, smooth, hummocky, smooth hummocky, and sedimented terrains, were visually identified on HR bathymetry and backscatter maps. Each is described below and in Table S1.

*Smooth terrain* is characterized by dominantly flat seafloor with higher backscatter than sedimented areas, which displays volcanic features, such as *lava flow fronts*, *lava tubes*, and *lava channels*. Lava flow fronts are associated with the edges of individual sequences of smooth lava flows (Figure 2d). Lava tubes are narrow and sinuous with different extents of collapse (Figure 2e), which is called uplifted tumuli (Appelgate & Embley, 1992). Lava channels have wider (up to 100 m) and sinuous depressions (Figure 2f).

*Hummocky terrain* has a rough topography with numerous individual *volcanic cones*. Volcanic cones are defined as cone-shaped volcanic edifices 2–415 m in diameter and up to 96 m in height (Figures 2b and 3b). Backscatter is generally high in hummocky terrain but patchy due to the rough relief. Hummocky terrains commonly occur as ridges, elongated sub-parallel to the ridge axis (e.g., l in Figure 2a).

*Smooth hummocky terrain* mixes the characteristics of hummocky and smooth terrains: rougher topography than smooth terrain but less so than hummocky terrain (Figure 2c). In the mapping of these terrains, we took scale into consideration: for example, in Figure 2c: flat seafloor in the center extends >500 m with very few volcanic cones and is therefore identified as smooth, while flat seafloor in the south is relatively elevated and extends <300 m between volcanic cones, leading to classification as smooth hummocky.



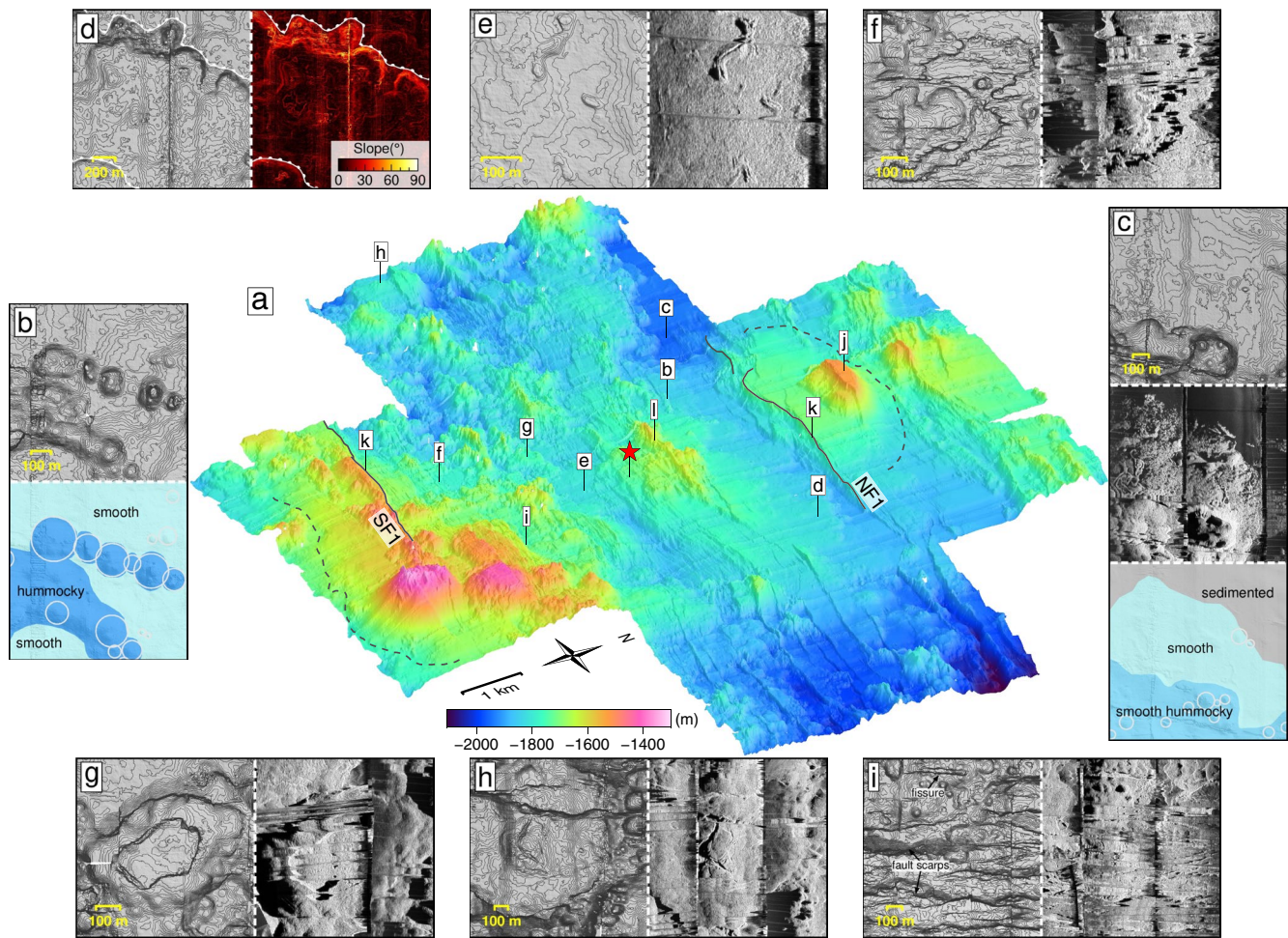


**Figure 2.** (a) 3-D view of high-resolution bathymetry at the center of the Southwest Indian Ridge 50°28'E segment, viewed from the ESE. Letters refer to locations of close-up views (b–i), and of features (j–l). Dashed lines show the approximate contour of the north and south flank of a rifted domal volcanic feature. Solid lines trace the top of conjugate fault scarps NF1 and SF1. Red star is the location of the Duanqiao hydrothermal field. (b) Example of seafloor morphologies for hummocky and smooth terrains (contours in 2 m and the same below). White circles represent volcanic cones. (c) Example of seafloor morphologies and backscatter for smooth hummocky, smooth, and sedimented terrains. (d) Lava flow fronts on smooth terrain in bathymetry (left) and slope (right) maps. (e) Lava tubes on smooth terrain in bathymetry (left) and backscatter (right) maps (the same below), with different extents of collapse (uplifted tumuli; Appelgate & Embley, 1992). (f) Collapsed lava channel with a dense network of fault scarps and fissures on smooth terrain. (g) Seamount with a central collapsed crater. (h) Seamount with a summit dome and radial fissures. (i) Dense network of fault scarps and fissures.

*Sedimented terrains* are characterized by flat seafloor with uniformly low backscatter (Figure 2c).

*Seamounts* are defined here as volcanic cones with diameters of >500 m (Searle et al., 2010). They can be flat-topped (j in Figure 2a), bowl-shaped, display collapsed *craters* (Figure 2g), or fissured summit domes (Figure 2h).

### 2.3.2. Fault Scarps and Fissures

Linear features, that is, *fault scarps* and *fissures*, were automatically detected from bathymetry, using the method by Panagiotakis and Kokinou (2015), then confirmed visually and digitized using backscatter and slope maps (Figure S1). Fault scarps are linear and correspond to sharp changes in bathymetry, slope, and backscatter (Figures 2f and 2i). Digitized fault scarps (Figure 4a) trace the scarp tops. Fissures correspond to narrow (<40 m) and linear depressions (Figures 2f, 2h and 2i). Digitized fissures trace the bottom of the fissure gaps. Fracture density (Figure 4b), including both fault scarps and fissures, was calculated as a kernel density with a grid size of 10 m and a search radius of 250 m.

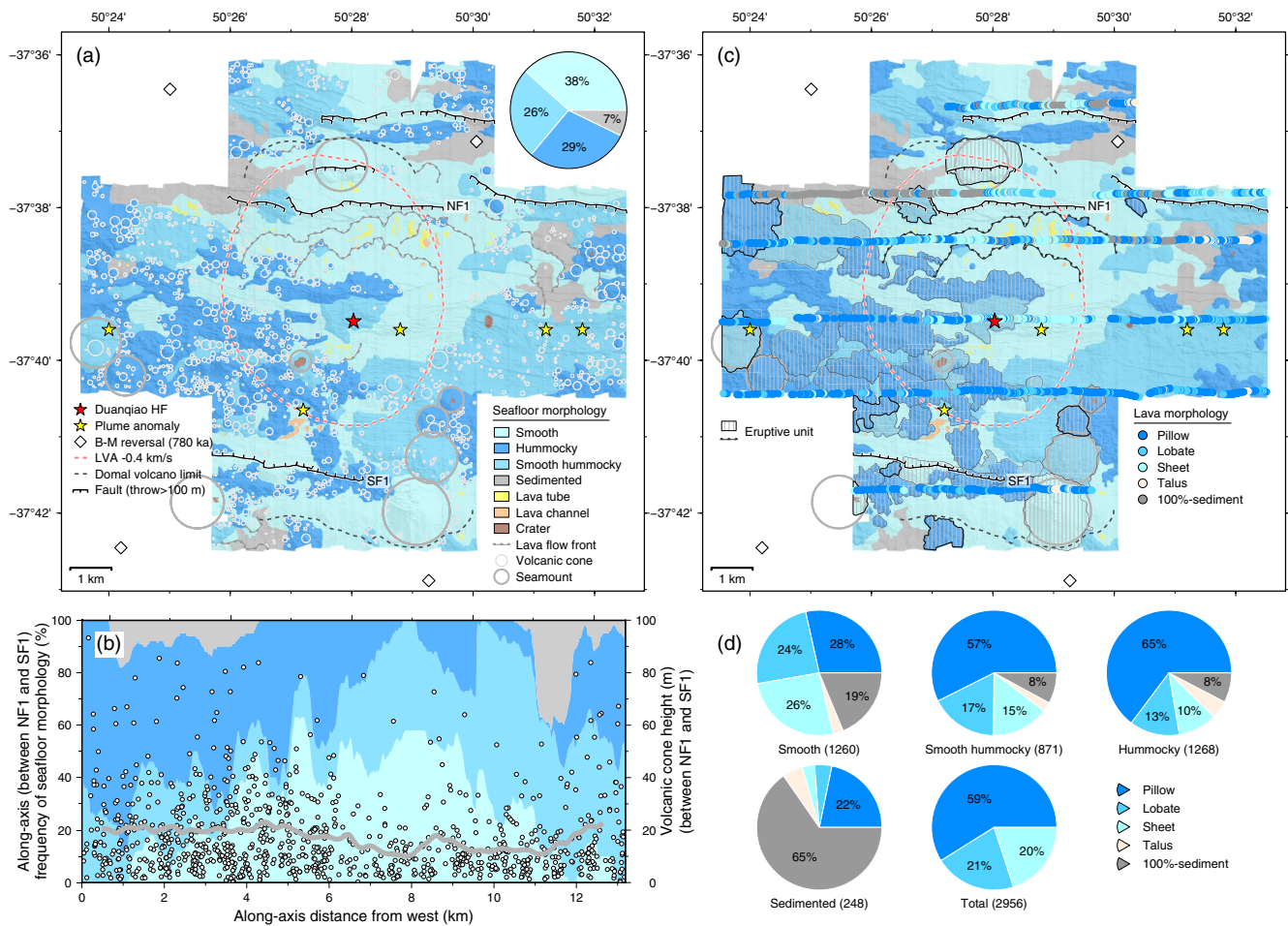


**Figure 3.** (a) Bathymetric interpretation in seafloor morphologies of smooth (38%), smooth hummocky (26%), and hummocky (29%) and sedimented (7%) seafloor, as well as lava tubes, lava channels, craters, volcanic cones, and seamounts. NF1 and SF1 are two conjugate normal faults. Dashed pink line outlines the *P* wave low-velocity anomaly of  $-0.4$  km/s at 7 km bsf (Jian, Chen, et al., 2017). Dashed black lines show the limit of the domal volcano, identified in Figure 2a. Red star is the location of the Duanqiao hydrothermal field. B-M reversal: magnetic anomaly pickings for B-M reversal (Sauter et al., 2009). (b) Along-axis statistics of seafloor morphology and volcanic cones between the conjugate NF1 and SF1. Lava tubes, lava channels, and craters are omitted in seafloor morphology. Circles indicate heights of individual cones. Thick gray line indicates the moving average of cone height with a window of 1 km and a step of 0.2 km. (c) Lava morphologies interpreted from seafloor photographs superimposed on the map of seafloor morphology. Pillow, lobate, and sheet lava, as well as talus and 100%-sediment are classified. 37 proposed eruptive units of hummocky ridges and seamounts are presented as closed and vertical-bar filled areas. Two proposed eruptive units of smooth lava flows are presented as unclosed lava flow fronts. (d) Proportion of seafloor photographs showing the distribution of lava morphologies on each type of seafloor morphology over the same transects. The normalized proportion in total is calculated by omitting photographs of 100%-sedimented seafloor and talus.

## 2.4. Tectonic Strain Estimation

Fault scarps and fissures exposed on the seafloor allow an estimation of the tectonic contribution to plate divergence at the upper crustal level, because successive lava flows potentially bury preexisting faults and fissures. This upper crustal tectonic strain is not necessarily representative of the tectonic strain at the scale of the axial lithosphere: upper-crustal faults and fissures may also form as a response to the emplacement of dikes that do not reach the seafloor (Rubin & Pollard, 1988). The tectonic strain was estimated on the basis of the measurements of vertical fault throw ( $D$ ) and fault dip ( $\alpha$ ) along axis-perpendicular profiles. Fault throw is defined as the depth difference between the top and bottom of the scarp, and its cumulative frequency theoretically fits an exponential distribution if the picking process provides a good record of small fault scarps (Deschamps et al., 2007). Because fault dip could be sharply decreased at the scarp bottom by the presence of mass wasting and/or post-faulting lava flows, the dip is defined as the largest value along the scarp. The cumulative horizontal fault heave ( $H$ ) along the profiles is calculated by the equation:



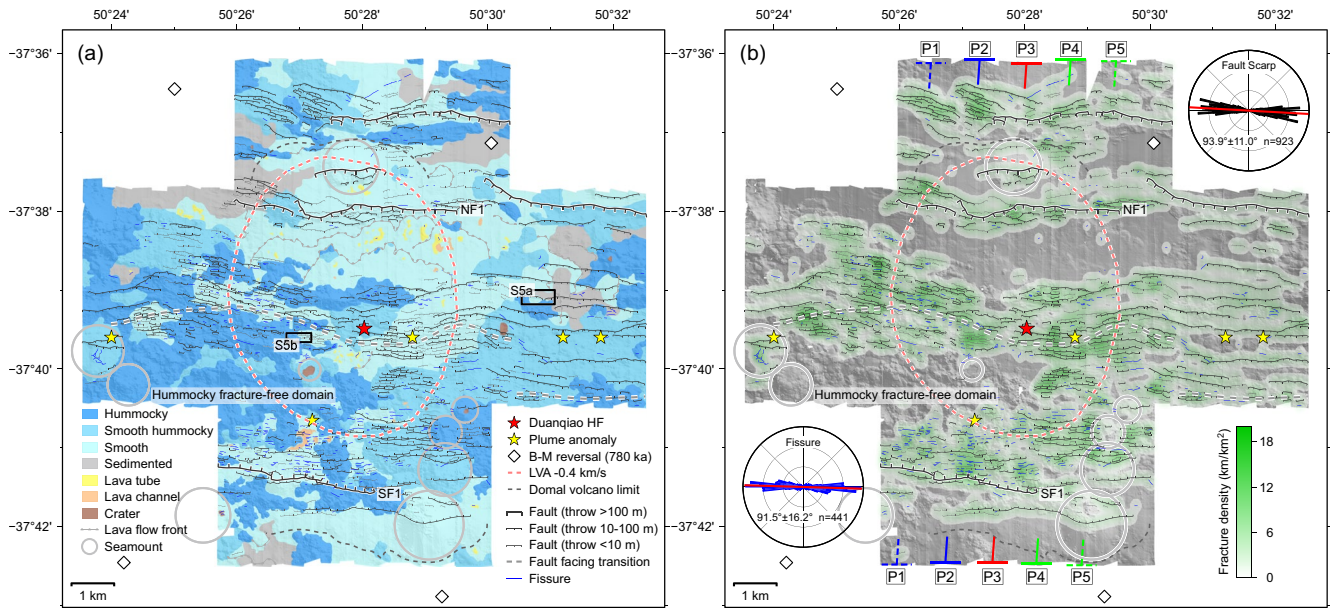


**Figure 4.** (a) Fault scarps and fissures superimposed on the map of seafloor morphology. Three categories of faults are shown, based on their maximum fault throw (>100, 10–100, and <10 m). Dashed gray lines indicate the locations of fault-facing transition, from north-facing (south of the axis) to south-facing (north of the axis). Red star is the location of the Duanqiao hydrothermal field. (b) Fracture density calculated as a kernel density with a grid size of 10 m and a search radius of 250 m. Rose diagrams indicate azimuth distribution of fault scarps (top right) and fissures (bottom left). Cross-axis profiles P1–P5 are used for estimating tectonic strain in Figure 6.

$$H = \frac{D}{\tan(\alpha)}$$

The tectonic strain ( $T_s$ ) along profiles is then calculated from the equation:

$$T_s = 100\% \times \frac{H}{L},$$

where  $L$  is the length of profiles. Fissures are neglected due to their small openings.

### 3. Results

The most prominent topographic features at the center of the SWIR 50°28'E segment are two elevated regions rifted by a pair of conjugate fault scarps with throws >100 m, NF1 and SF1 (k in Figure 2a). These elevated regions include several large seamounts (e.g., j in Figure 2a) that rest on a rifted domal structure (dashed lines in Figure 2a). The contours of this domal structure are more visible in the northern flank. They are obscured in the southern flank by a large seamount and several hummocky ridges (Figure 2a). Several flat-topped seamounts have been dissected by normal faults, with one half still visible (e.g., j in Figure 2a). Seamounts are less frequent in the near-axis region between fault zones NF1 and SF1, where the dominant topographic features are axis-parallel hummocky ridges and low-throw fault scarps (Figure 2a). In this near-axis region, there is no clear contrast in backscatter (Figure 1c) that would indicate where the most recent eruptions have occurred. In the following paragraphs, we analyze the distributions of the map-scale seafloor morphologies, photo-scale lava morphologies, eruptive units, and fault scarps and fissures (Figures 3 and 4).

#### 3.1. Distribution of Map-Scale Seafloor Morphologies

The smooth seafloor morphology represents 38% of the total AUV-mapped area, smooth hummocky morphology 26%, hummocky morphology 29%, and sedimented seafloor 7% (Figure 3a). The smooth morphology covers vast expanses of the seafloor, particularly in the center and north parts of the map. The smooth hummocky morphology covers most of the relatively lower backscatter region in the south-eastern part



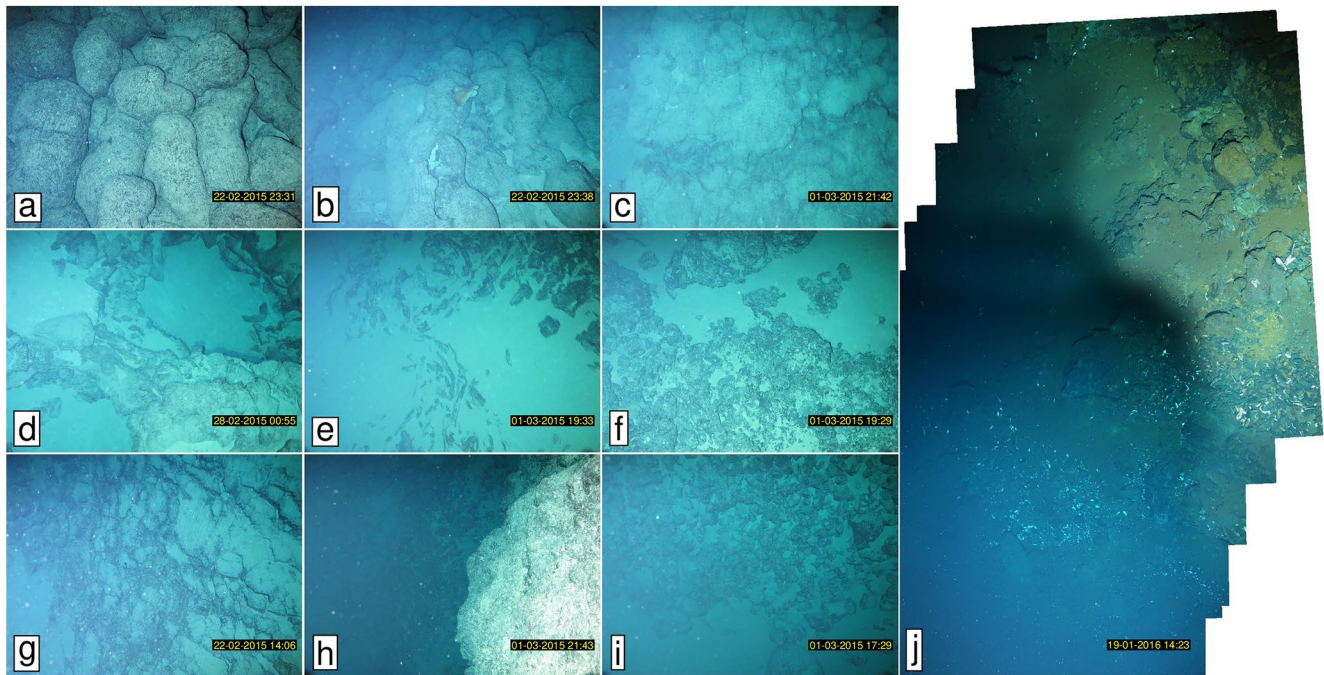


**Figure 5.** Representative seafloor photographs for lava morphologies and features (a–i) by deep-tow camera; (j) by autonomous underwater vehicle camera. (a) Pillow lava; (b) Elongated pillow lava on steep flanks; (c) Lobate lava; (d) Collapsed lobate lava; (e) Folded sheet lava; (f) Hackly sheet lava; (g) Broken sheet lava; (h) Fault scarp; (i) Talus with rubble; (j) Sulfide and dead mussel around the Duanqiao hydrothermal field.

of the map. The hummocky morphology is more abundant in the west of the map and is associated with elongated ridges and isolated patches of seafloor that are more elevated than their surroundings. Sedimented seafloor mainly occurs in the distal parts of the mapped area. The density of volcanic cones in the entire mapped area is  $13.9/\text{km}^2$  with a total of 1,529 cones, and this value increases from smooth ( $4.2/\text{km}^2$ ), smooth hummocky ( $17.2/\text{km}^2$ ), to hummocky ( $26.9/\text{km}^2$ ) morphologies. The average cone height in the map is 17.2 m, with the same trend increasing from smooth (8.0 m), smooth hummocky (12.4 m), to hummocky (22.1 m) morphologies.

Along-axis statistics of seafloor morphology and volcanic cones in the near-axis region between conjugate fault zones NF1 and SF1 are shown in Figure 3b. Smooth and smooth hummocky seafloor (>70%) are dominant within a ~5 km-long central domain (6–11 km in Figure 3b), while hummocky seafloor becomes prevalent to the east and west of this central domain. The distribution of volcanic cones is coincident with this trend of seafloor morphology: lower cone density and height (mostly <20 m) in the central domain, and larger cone density and height (2–96 m) outside this domain (Figure 3b).

### 3.2. Distribution of Photo-Scale Lava Morphologies

Lava morphologies (pillow, lobate, and sheet lavas) were identified from seafloor photographs along six ridge-parallel transects (Figures 3c and 5). The distribution of lava morphologies is consistent with the seafloor morphologies identified from HR mapping over these six transects (Figures 3c and 3d). Smooth terrain along the documented transects is characterized by 50% lobate-sheet lavas and 28% pillow lavas, while hummocky terrain is mainly composed of pillow lavas (65%) with only 23% lobate-sheet lavas (the rest are talus or sediments). Smooth hummocky terrain has 57% pillows and 32% lobate-sheet lavas. Seafloor mapped as sedimented corresponds to seafloor photographs that show 65% are fully covered by sediment, the rest being made up of heavily sedimented pillows, lobate lava or sheet lavas (Figure 3d). Omitting photographs of talus and complete sediment cover, the normalized proportions of pillow lava and lobate-sheet lava flows are 59% and 41%, respectively, along the six investigated transects (Figure 3d).

### 3.3. Eruptive Units

Thirty nine eruptive units are proposed in Figure 3c. Most (29) correspond to small hummocky ridges or portions of larger hummocky ridges, for which contrasts in morphology or seafloor reflectivity suggest a chronology in volcanic construction. The eight mapped seamounts are also identified as eruptive units. The remaining two eruptive units are successive sequences of smooth terrain bounded by 15–75 m high, lobate, and up to 8 km-long lava flow fronts, that are located just south of fault zone NF1 (Figure 2d).

### 3.4. Pattern of Fault Scarps and Fissures

Nine hundred twenty-three fault scarps and 441 fissures were recognized in the HR bathymetry map (Figure 4). Seafloor photographs show talus at the base of some fault scarps (e.g., Figure 5h). Fault scarps were classified into three groups according to their maximum throws: >100, 10–100, and <10 m (Figure 4a). The larger fault scarps include the conjugate NF1 and SF1. Individual fault scarps extend 0.05 to >4 km. NF1, and SF1, the most prominent fault scarps, are comprised of several individual faults (Figure 4a). Fissures are 20–530 m long, up to 38 m wide and up to 20 m deep. They are more abundant in smooth and smooth hummocky seafloor than in hummocky seafloor. Cumulative frequency of lengths of fault scarps and fissures fit exponential laws (Figure S4).

The average fault orientation is  $93.9^\circ \pm 11.0^\circ$ , roughly orthogonal to the spreading direction, and the average fissure orientation is  $91.5^\circ \pm 16.2^\circ$  (Figure 4b), the higher deviation is due to radial fissures in volcanic edifices (e.g., Figure 2h). Fault scarps are dominantly south-facing in the north and north-facing in the south of the mapped area, and the transition, that is, the location of ridge axis from the point of view of surface tectonics, is located at the latitude of the Duanqiao HF, except to the east of  $50^\circ 30' E$ , where it is offset to the south by  $\sim 1.5$  km (Figure 4a). Close examination of the HR bathymetry and slope maps reveals age relationships between faulting and lava emplacement: some fault scarps cut through preexisting seafloor, while others are partially buried by later lava flows (e.g., Figure S5).

The fracture density varies between 0 and 18 km/km<sup>2</sup> in the mapped area (Figure 4b), and the average density is  $\sim 3$  km/km<sup>2</sup>. Three relatively broad ridge-parallel domains are fracture-free: A 1.3–2 km-wide, smooth domain with the two well-preserved lava flow fronts south of the NF1 scarp, a >1 km-wide mostly smooth domain in the southernmost part of the mapped area, and a 1.3–1.8 km-wide and 6 km-long hummocky domain to the south and southwest of the Duanqiao HF (Figures 4a and 4b). This fracture-free hummocky domain does not extend into the eastern part of the map, but ends eastward into an extensively faulted domain of smooth hummocky terrain.

### 3.5. Tectonic Strain

Based on the pattern of faulting, the surface tectonic strain was estimated along five axis-perpendicular profiles (P1–P5 from west to east in Figure 4b). Cumulative fault throws along each profile were measured between the northern and southern extremities (Figure 6a), and between the bottoms of the conjugate NF1 and SF1 fault scarps (Figure 6b). The cumulative frequency of fault throw fits an exponential law (Figure 6c). Individual fault scarps have dips between  $30^\circ$  and  $80^\circ$  (95% confidence interval; sketch of the measurements shown in the inset of Figure 6a), and have mean dip values of  $55^\circ$ – $65^\circ$ . The calculated apparent tectonic strain over the whole length of the five profiles, ranges between 4.4% and 7.7% for a fault dip of  $55^\circ$ , and 3.6% and 5.1% for a fault dip of  $65^\circ$  (Figure 6a). Between the conjugate NF1 and SF1 scarps, tectonic strain ranges between 2.6% and 13.4% for a fault dip of  $55^\circ$ , and 1.8% and 8.9% for a fault dip of  $65^\circ$  (Figure 6b). Profile P4, near the eastern tip of the fracture-free hummocky domain (Figure 4b), yields the maximum tectonic strain.

### 3.6. Near-Bottom Magnetic Anomalies

The two AUV magnetic profiles are located in the center of the study area (Figures 1b and 7a). To the north, they extend over the location of the B-M reversal as picked from sea-surface magnetic anomalies (magnetic A1 in Figure 1a; Sauter et al., 2009). This anomaly corresponds to clear lows in both near-bottom magnetic profiles (Figure 7b). The two profiles, distant by 0.8 km, record similar patterns of magnetic anomalies:

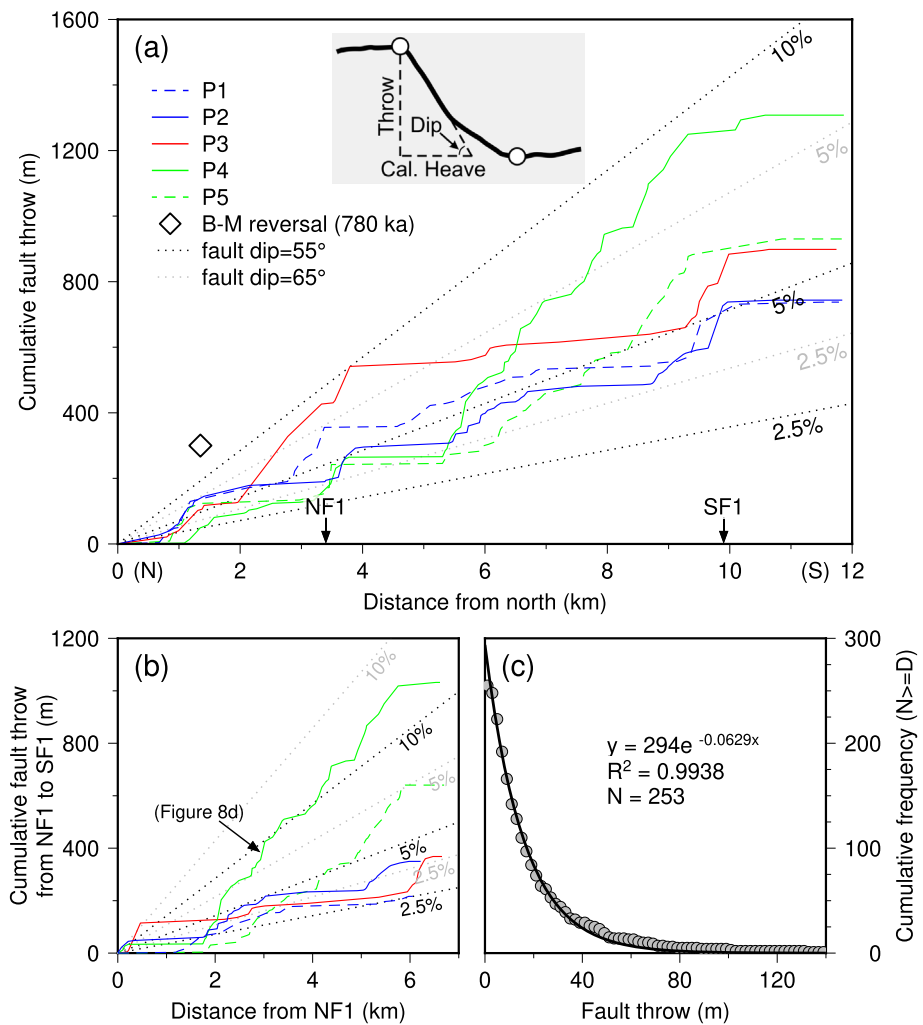


**Figure 6.** (a) Cumulative fault throw measured between the northern (0 km) and southern extremities along five profiles (P1–P5) located in Figure 4b. Fissures are neglected. Black and gray dotted lines represent the estimation using fault dips of 55° and 65°, respectively, for tectonic strain of 2.5%, 5%, and 10%. The definitions of throw, maximum dip, and calculated heave of fault scarp are shown in the inset sketch. (b) Cumulative fault throw measured between the bottoms of conjugate NF1 and SF1. (c) Cumulative frequency of fault throw ( $N \geq D$ ) binned by 2 m along five profiles (P1–P5). The exponential fit follows a law of the form:  $y = 294e^{-0.0629x}$ , with the correlation coefficient ( $R^2$ ) of 0.9938.

Magnetic highs are located outward from the conjugate NF1 and SF1 scarps, while magnetic lows are found inward of these two scarps (Figure 7b). The hummocky fracture-free domain corresponds to magnetic highs (red arrows in Figure 7b). The highly fractured domain to the north of this fracture-free domain corresponds to a magnetic low, while the smooth fracture-free domain with the two lava flow fronts (Figure 2d), and hummocky ridge on top of it (1 in Figure 2a) correspond to weak magnetic anomalies (Figure 7b).

#### 4. Discussion

Our results provide new insights into volcanic and tectonic processes at the center of the magmatically robust SWIR 50°28'E segment. These results inform the spatial and temporal evolution of upper-crustal construction since the B–M reversal, ca 780 kyr ago (Cande & Kent, 1995). We propose an interpretation of this evolution, calling for phases of waxing and waning magmatic activity. We then examine the implications of our findings for the relation between upper-crustal construction and magmatic activity in the global MOR.



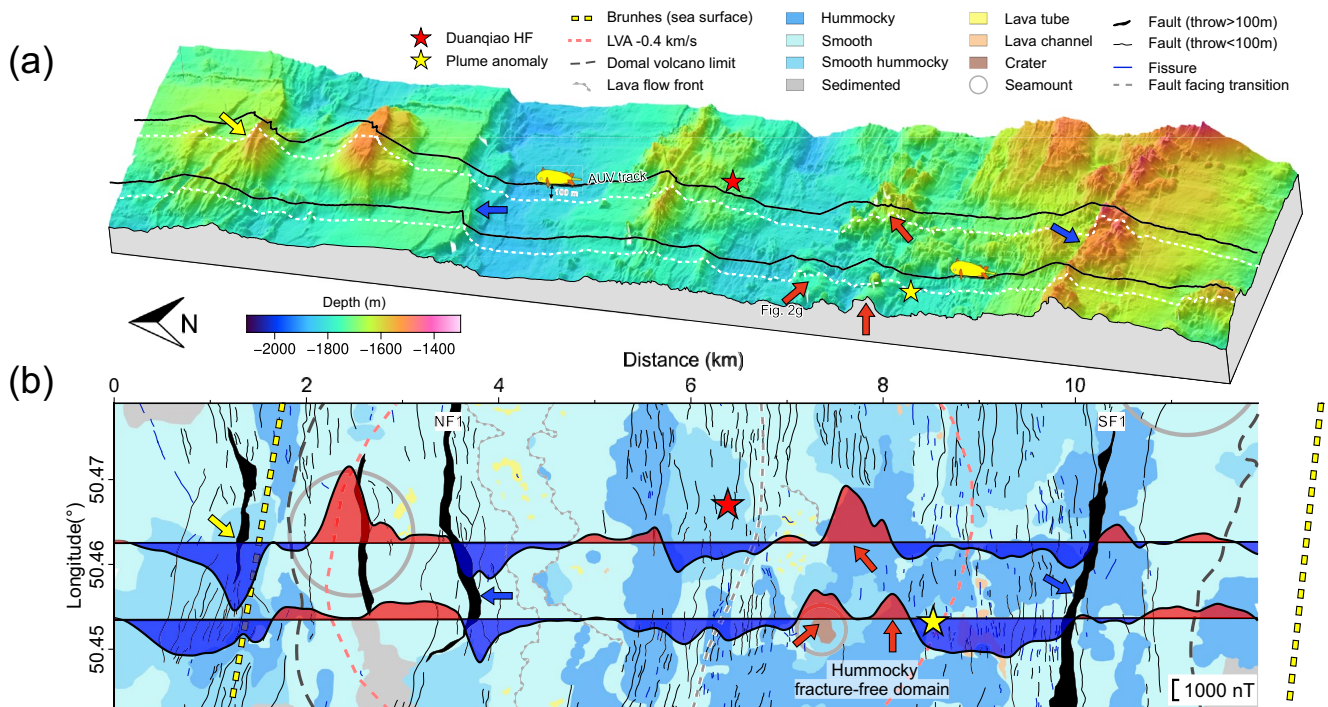


**Figure 7.** (a) 3-D seafloor topography with tracks of autonomous underwater vehicle (AUV) survey ~100 m above the seafloor at a velocity of 1–2 kt. Yellow, blue, and red arrows respectively mark the interpreted locations of Brunhes, the conjugate NF1 and SF1, and the most recent hummocky eruptions. Red star is the location of the Duanqiao hydrothermal field. (b) Total magnetic anomaly plotted along AUV track lines, superimposed on geological interpretation (after Figure 4a). Reduction-To-Pole was applied to locate the magnetic anomalies above their sources.

#### 4.1. 780 kyr of Upper-Crustal Construction at the Center of the Magmatically Robust SWIR 50°28'E Segment

##### 4.1.1. Eruptive Phases and Modes of Upper-Crustal Construction

Based on the mapped seafloor morphologies, eruptive units, and faults distribution, we propose that the upper crust formed at the center of the SWIR 50°28'E segment has experienced at least six eruptive phases, V0–V5, within the past 780 kyr (Figure 8a). V0 corresponds to the construction of the upper crust on which the smooth domal volcano that is, now rifted to the north of NF1 and to the south of SF1 (dashed lines in Figures 2a and 8a) was built. A faulted flat-topped seamount that is, partially covered by smooth lava to the north of NF1 (j in Figure 2a), could have formed during the V0 phase. The V1 domal volcano (Figure 8b) originally had a diameter of 5–8 km. Its contours are now obscured in the south by several younger hummocky ridges and seamounts (Figures 2a and 8a). We interpret these as having formed during the V2 eruptive phase, together with the rifting of the V1 domal volcano along the conjugate NF1 and SF1 fault zones (Figures 8a and 8c). This “split-volcano” configuration is commonly observed in the center of magmatically robust slow and ultraslow spreading ridge segments (Escartín et al., 2014).

V1 is interpreted as a phase of high magma supply. The prevalence of smooth lava flows in the V1 domal volcano points to elevated eruptive rates, with feeding dikes centered within a narrow injection zone (Figure 8b). By contrast, V2 corresponds to the formation of several hummocky ridges and seamounts and the rifting of the V1 domal volcano. This points to lower eruptive rates during individual eruptions, to a wider zone of dike injection (Figure 8c), and to a more significant tectonic contribution to plate divergence. We, therefore, relate the transition from V1 to V2 to a waning magma supply. Early V2 volcanic constructions are mostly found in the southern flank of the rifted V1 domal volcano (Figure 8a). After the initial stages depicted in Figure 8c, the V2 eruptive phase presumably built the substratum for the lava flow fronts that are visible to the south of the NF1 scarp (Figures 2d and 8a). These lava flow fronts were formed during the V3 eruptive phase, and they bound eruptive units that extend up to 2 km downslope from their eruptive sources (inferred to have been located near a later hummocky ridge, marked as l in Figure 2a). It is likely that these

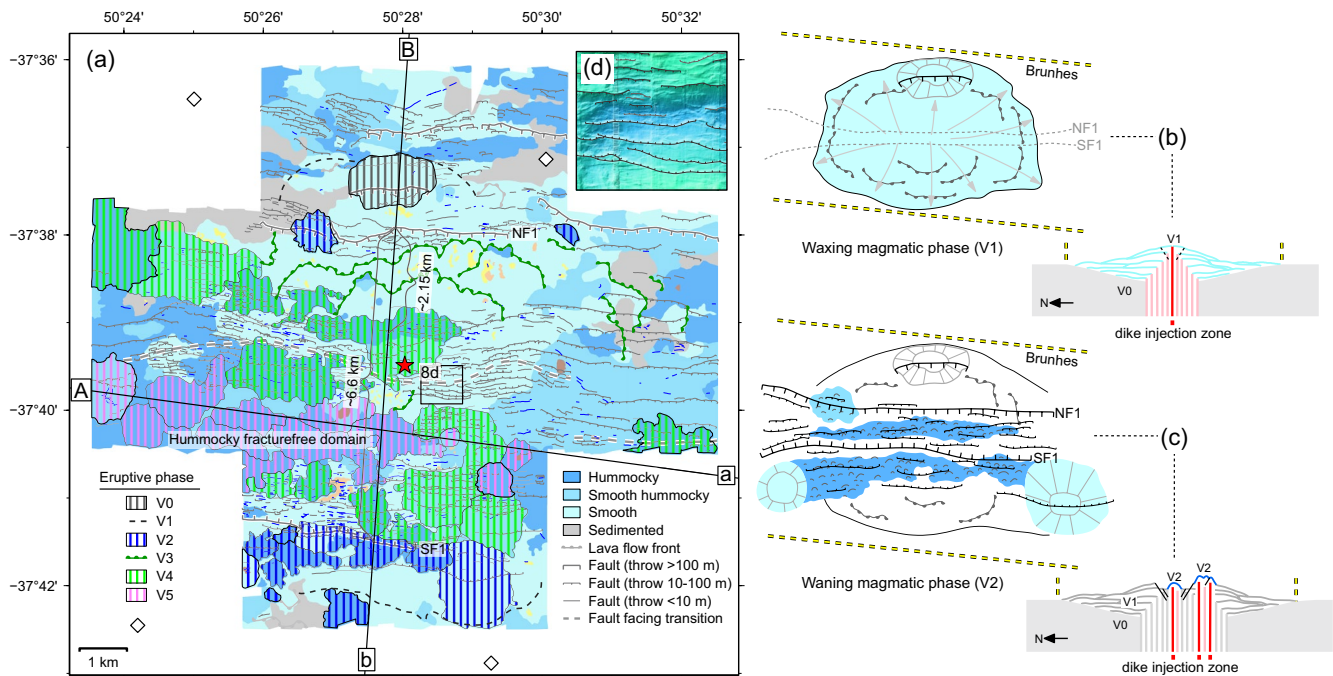


**Figure 8.** (a) Interpretative map showing the distribution of eruptive units for the six proposed eruptive phases of upper-crustal construction (V0 to V5 from older to younger), superimposed on the geological map (after Figure 4a). Profiles A-a and B-b, along and across the most recent eruptive phase V5, refer to the locations of seismic profile in Figures 9a and 9b, respectively. Red star is the location of the Duanqiao hydrothermal field. (b) Sketches showing the construction of the domal volcano toward the end of magmatically robust eruptive phase V1. In cross section, the most recent feeding dikes are in red, previous dikes in pink or gray. (c) Sketches showing the early stage of less magmatically robust eruptive phase V2. (d) Close-up view of the central, narrow graben (location in Figure 8a). See text in Section 4.1.1 for explanation.

smooth lavas also flowed to the south during V3, and currently form the substratum for later lava flows. The predominance of smooth lava, flowing significant distances from a localized inferred eruptive source, is similar to the V1 phase (Figure 8b) and suggests that V3 was a phase of renewed (waxing) magma supply.

The hummocky ridge that tops the V3 lava flows (l in Figure 2a) suggests lower effusion rates. We attribute its formation to the onset of the V4 eruptive phase, characterized by a waning magma supply. Similar to what happened during the V2 waning phase, V4 eruptions appear to have mainly occurred to the south, so that the V3 seafloor was preserved only in the north (Figure 8a). The chronology of volcanic phases is more difficult to unravel in the 4.4 km-wide domain between the early V4 hummocky ridge (l in Figure 2a) and the SF1 fault zone (Figure 8a). The seafloor there is significantly fractured, with the notable exception of the hummocky fracture-free domain to the south and southwest of the Duanqiao HF (Figures 4a and 4b). This elongated, ridge-parallel, and fracture-free domain also corresponds to magnetic highs (Figure 7b). We propose that it is the product of the most recent, V5, eruptive phase. This V5 hummocky fracture-free domain ends eastward into extensively fractured smooth hummocky seafloor that probably formed during V4 (Figure 8a). Most scarps in this fractured area face to the north at the latitude of the hummocky fracture-free domain, then face to the south just 1 km to the north at the latitude of Duanqiao HF. We interpret the resulting narrow graben (Figure 8d) as being due to recent tectonically accommodated plate divergence in the mapped area. Therefore, the most recent spreading would be mostly magmatic in the west and tectonic in the east.

The spatial distributions of eruptive products indicate that eruptive centers during magmatically robust (waxing) phases V1 and V3 were located near the center of the mapped area, just north of the latitude of the Duanqiao HF. By contrast, during less magmatically robust (waning) phases V2, V4, and V5, most eruptions occurred in the south, near the latitude of the hummocky fracture-free domain.

#### 4.1.2. Constraints on Crustal Ages

The B-M reversal, at 780 kyr, is identified in sea-surface (Sauter et al., 2009) and in near-bottom magnetic anomalies (Figure 7b), providing the strongest constraint on crustal ages in the mapped area. Its traces on the south and north plates are separated by  $\sim 11$  km, consistent within error to the  $\sim 14$  mm/yr regional spreading rate (Patriat et al., 2008). This leads to interpret the maximum age of the onset of V0 phase (near the B-M reversal) as 780 kyr (Figure 8a). The next age constraint comes from the distance between the conjugate NF1 and SF1 scarps, which we interpreted as having initiated near the top of the V1 domal volcano (Figure 8b). This distance, 6.6 km (Figure 8a), would suggest a spreading age of  $\sim 471$  kyr, corresponding to the onset of the V2 phase. However, parts of V2 eruptive products were emplaced on V1 seafloor (to the south of SF1 in Figure 8c), and their corresponding plate divergence, which is unknown, should be added to the 6.6 km to get a more accurate spreading age for the onset of the V2 phase.

The age of the onset of the next magma waning phase (V4) can be estimated based on the 2.15 km across-axis distance between the early V4 hummocky ridge (l in Figure 2a) and the top of the NF1 scarp (Figure 8a). This suggests a total duration of 307 kyr for V2 and V3 together, and an age of 164 kyr for the onset of V4. The age of the onset of V5 is tentatively estimated as only 19 kyr, based on the cumulative heave of fault scarps of 0.27 km (calculated for a fault dip of  $55^\circ$ ; Figure 6b) within 1 km to the north and south of the small graben shown in Figure 8d. This is one order of magnitude lower than the total estimated duration of V4 + V5 (164 kyr), so that it seems more consistent to interpret V5 as just the most recent episode of the V4 eruptive phase.

#### 4.1.3. Cycles of Magmatic Activity

Our interpretation of the eruptive phases associated with the past 780 kyr of plate spreading at the center of the SWIR  $50^\circ 28' E$  segment, involves significant changes in magma supply, with alternating periods of more robust, waxing magmatism (V1 and V3), and of less robust, waning magmatism (V2 and V4 + V5). Age constraints suggest a periodicity of about 300 kyr for these variations: up to 310 kyr from the start of V0 to the start of V2, and 307 kyr from the start of V2 to the start of V4.

Mendel et al. (2003) used the width of abyssal hills off-axis from our study area (Figure 1a), to propose a longer period (2–3 myr) magmatic cyclicality. These abyssal hills are interpreted as large split axial volcanos and correspond to changes of  $\sim 1$  km in gravity-derived crustal thickness (Mendel et al., 2003). These 2–3 myr-long magmatic cycles occurred at the apex of a regional mantle melting anomaly, which is currently at its waning stage (Sauter et al., 2009). Our fine-scale geological observations document shorter magmatic cycles that occur during this waning stage, and with no detectable changes in crustal thickness, as revealed by the across-axis seismic velocity profile A-A' in Figure 1a (Jian, Chen, et al., 2017). Since crustal construction is a protracted process with more recent eruptions piling up over older seafloor (Figures 8b and 8c), and because of the very slow spreading rate, this is likely to dampen crustal thickness variation signals with periods of only a few 100s kyr.

Magmatic cycles with periods of the same order of magnitude have been documented at other sections of slow to ultraslow spreading ridges. At  $19^\circ S$  on the slow-spreading Central Indian Ridge, cyclic variations in basalt geochemistry suggest magmatic cycles of 150–200 kyr (Cordier et al., 2010). The cyclic occurrence of off-axis topographic highs at the Menez Gwen segment of the slow-spreading MAR points to magmatic cycles of 300–500 kyr (Klischies et al., 2019). At the ultraslow-spreading SWIR, melt replenishment cycles occurring over 180–250 kyr were proposed based on zircon dating of the gabbroic sequence drilled (ODP Holes 735B and 1105A) at the Atlantis Bank (Rioux et al., 2016). These cycles could be controlled by compaction processes in the melt-rich mantle below the ridge, or in the lowermost-crustal mush zone (Cordier et al., 2010; Rabinowicz & Toplis, 2009).

## 4.2. Upper-Crustal Construction and the Magma Plumbing System

In Figure 9c, we propose a conceptual sketch to relate the recent upper-crustal construction documented in this study, to the deeper characteristics of the axial magma plumbing system, based on seismic velocity (Jian, Chen, et al., 2017; Jian, Singh, et al., 2017) and microseismicity (Yu et al., 2018) constraints. The boundary between the upper and lower crust that is, layers 2 and 3, is defined by a vertical velocity gradient



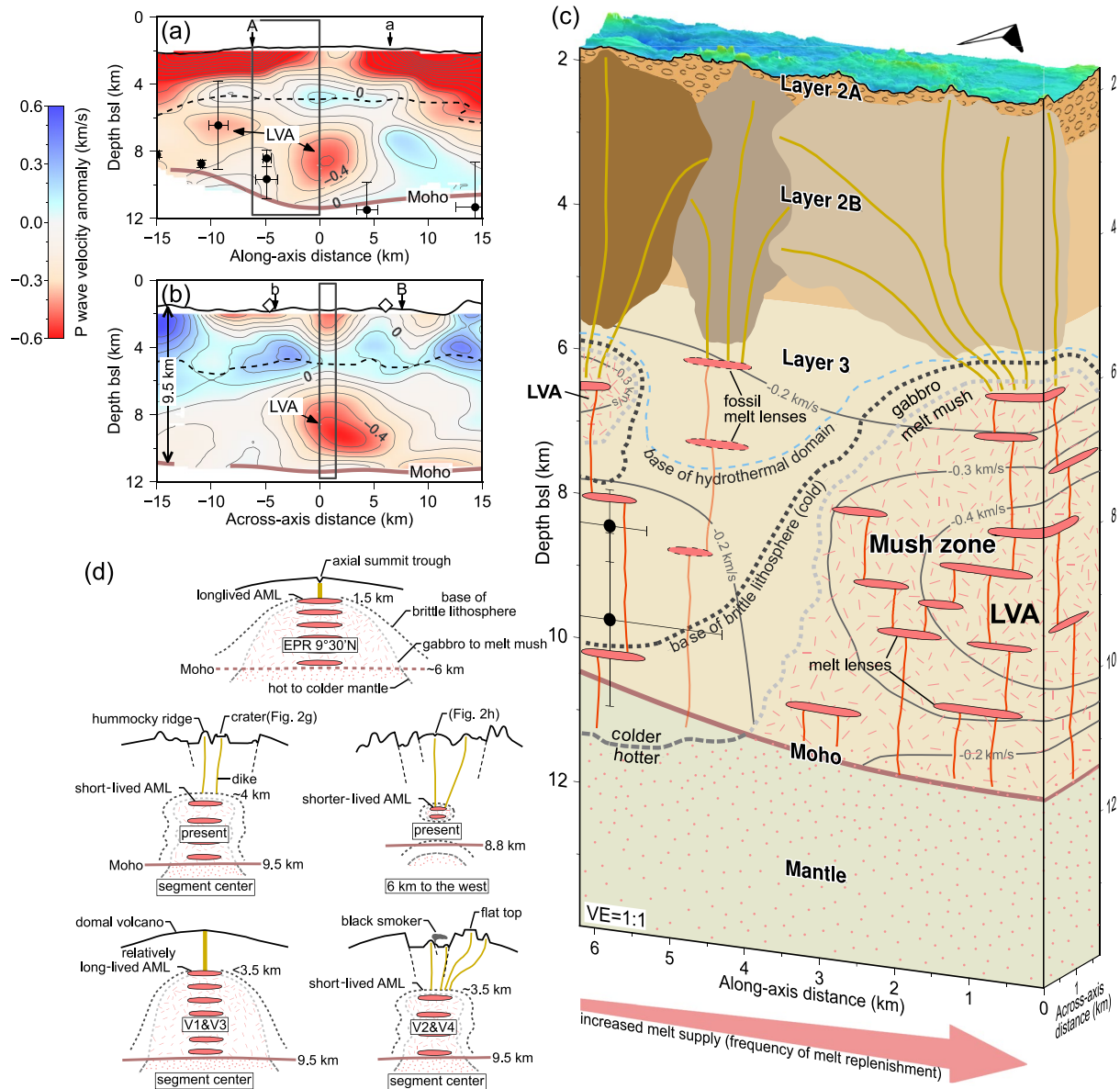


**Figure 9.** *P* wave velocity anomaly along (a) and across (b) the recent eruptive phase V5 (contours in 0.1 km/s), data extracted from 3-D seismic tomography (Jian, Chen, et al., 2017). Locations of A-a and B-b are shown in the map of Figure 8a. Dashed lines are the boundary of crustal layers 2 and 3, defined by the vertical velocity gradient of 0.3 s<sup>-1</sup> (Jian, Chen, et al., 2017). Moho interface based on PmP arrivals is shown as thick brown lines (Jian, Chen, et al., 2017). Two low-velocity anomalies are shown at segment center within the lower crust (minimum <math>-0.6</math> km/s) and in the west within the mid crust (minimum <math>-0.35</math> km/s), respectively. Black dots with error bars indicate the hypocenters of microearthquakes (Yu et al., 2018). Closed squares outline the area of the 3-D model in Figure 9c. (c) Magma plumbing system for the recent eruptive phase (V5) showing the topography, crustal structure, dike injection, mush zone, mantle, and thermal structure, constrained by seismic velocity and microseismicity (Jian, Chen, et al., 2017; Yu et al., 2018). Vertically stacked melt lenses connected by dikes are inferred in the hot lower-crustal mush zone. Dots and dashes indicate crystal mushes. (d) Sketches showing magma plumbing systems for EPR 9°30'N, the present-day center of the SWIR 50°28'E segment and 6 km to the west to the segment center, and segment center during V1&V3 and V2&V4. See text in Sections 4.2 and 4.3 for explanation.

of 0.3 s<sup>-1</sup>, and the Moho interface is defined by PmP arrivals (Jian, Chen, et al., 2017). Based on the full waveform inversion results of Jian, Singh, et al. (2017), we propose that the LVA documented beneath the SWIR 50°28'E segment center (Figures 9a and 9b), corresponds to partially crystallized gabbro, at temperatures greater than 1,000°C and with residual melt contents increasing from less than 10% at a depth of 4 km bsf, to probably greater values in the LVA center. We tentatively draw the contours of this hot and melt-bearing domain down to Moho depth, where we propose that it roots into the melt-bearing upper

mantle (Figure 9c). Inspired by observations of stacked melt sills at fast and intermediate spreading ridges (Carbotte et al., 2020, 2021; Marjanović et al., 2014), and by a conceptual model of the transcrustal magma plumbing system beneath subaerial volcanos (Cashman et al., 2017), we also propose that some of the melt in this hot lower crustal region resides in vertically stacked melt lenses (Figure 9c), and that these lenses play a role in transferring melt from the mantle to the upper crust to feed eruptions. In Figure 9c, we also infer that most hydrothermal cooling occurs in a domain that is, limited both by temperature (ca 600°C) and pressure (corresponding to depths <6 km) as proposed by Morgan and Chen (1993). This limit is not meant to define the base of the fluid penetration in the lithosphere, but the domain of potentially vigorous hydrothermal circulation.

Moving just a few kilometers away from the hot central LVA region toward the ridge segment ends, we infer, based on the lateral increase of seismic velocities (Jian, Chen, et al., 2017), that lower crustal temperatures drop laterally below the solidus, yielding solidified and cooled gabbros. A smaller LVA, which we similarly interpret as a melt-mush zone, is documented in the shallow lower crust, ~6 km to the west of the segment center (Figure 9a; Jian, Chen, et al., 2017). This small mid-crustal mush zone is located just below, and may have fed, the fissured, dome-topped seamount (Figure 2h). In Figure 9c, we follow the implicit interpretation of Yu et al. (2018) that the mid-segment axial earthquakes are tectonic, and therefore reveal an along-axis deepening of the brittle lithosphere to the west. If these events are in fact magmatic, corresponding to diking associated with melt transport through the crust, the thermal regime need not be that cold beneath the smaller, western LVA.

The present-day along-axis configuration sketched in Figure 9c is heterogeneous, with significant variations in the thermal regime over distances of a few kilometers, which we propose are directly related to along-axis variations in the recent history of melt supply, and more specifically of the replenishment rates in the lower-crustal magma plumbing system of melt mush and stacked melt lenses (Figure 9c). This interpretation emphasizes the role of melt supply variations as a control of the thermal regime of slow and ultraslow spreading ridges (Cannat et al., 2019). Frequent melt replenishment keeps the lower crust hot, pushing up the base of the brittle lithosphere and the base of the hydrothermally cooled domain (Fan et al., 2021). Less frequent melt replenishment results in deep and shorter-lived AMLs, a thicker brittle domain, and more variable but generally deeper hydrothermal circulation (Figure 9c).

The whole segment at 50°28'E is a magmatically robust endmember for the ultraslow spreading SWIR. The configuration sketched in Figure 9c corresponds to a relatively large time-averaged melt supply, enough to make a magmatic crust  $\geq 8.8$  km-thick (Figure 9a). The contrasted present-day, across-axis settings in Figure 9d, one for the main LVA region at the segment center, and the other for the smaller, mid-crustal LVA region 6 km to the west of the segment center, corresponds to a relatively low melt supply. They likely prevailed during the most recent eruptive phase, forming the V5 hummocky ridges and seamounts, as part of the V4-V5 magma supply waning phase. We propose that the axial thermal regime and magma plumbing system was similar during the other documented magma waning phase (V2), with short-lived AMLs above shrinking mush zones (Figure 9d). Waxing phases V1 and V3, forming domal volcanos with predominantly high-effusion-rate smooth and smooth hummocky lava, probably corresponded to hotter axial regimes, with larger volumes of melt readily accessible in shallower, more frequently replenished, and thus relatively long-lived AMLs (Figure 9d). These relatively long-lived AMLs probably resided at depths shallower than the top of the current mush zone at ~4 km bsf (Jian, Singh, et al., 2017), or than the AML depth at the center of the MAR Lucky Strike segment (Comber et al., 2015; Singh et al., 2006), which is currently experiencing the early stages of rifting of a domal volcano formed during a more magmatically robust recent phase of spreading (Escartín et al., 2014; Humphris et al., 2002).

### 4.3. Implications for the Modes of Upper-Crustal Construction and Magma Plumbing Systems at MORs

Our model for the magma dynamics of the melt-rich SWIR 50°28'E segment suggests cyclic variations in both the modes of upper-crustal construction (construction of a domal volcano with a localized dike injection zone, or predominance of hummocky ridges with a broader dike injection zone; Figures 8b and 8c) and the magma plumbing system (relatively long-lived and frequently replenished AMLs above broad melt mush zones, or shorter-lived AMLs on top of narrower and shrinking mush zones; Figure 9d). We now

extend this model to a comparison with other well-documented magmatically robust ridge sections where both HR bathymetry data and seismic data are available.

Fast spreading ridges, like the EPR 9°30'N, are characterized by a predominance of high-effusion-rate smooth lava flows (Fundis et al., 2010), fed by a dike injection zone that is, mostly localized in a few 100s meters-wide Axial Summit Trough (Fornari et al., 1998). The hotter thermal structure of the EPR at 9°30'N (Figure 9d) is nearly 2D and steady-state, with a 1.5 km-deep, long-lived AML on top of a mush zone (Detrick et al., 1987; Dunn et al., 2000) that contains stacked melt lenses (Marjanović et al., 2014).

Intermediate spreading ridges tend to have variable lava morphologies (Figure S6a), from Axial Seamount at the Juan de Fuca Ridge with smooth-dominated lava flows and a shallow AML similar to that of fast-spreading ridges (Arnulf et al., 2018; Clague et al., 2017), to GSC 95°W with a prevalence of hummocky seafloor and no detectable AML (Blacic et al., 2004; Colman et al., 2012).

Slow and ultraslow spreading ridges have a yet larger spectrum of upper-crustal construction modes and magma plumbing systems. Ridge sections with moderate and low melt supply are typically characterized by hummocky ridges (e.g., Cann & Smith, 2005; Searle et al., 2010), with no detectable AML (Detrick et al., 1990). At melt-rich segments, the construction of smooth domal volcanos at segment centers corresponds to a local AML and/or crustal melt mush zone, such as at the MAR Lucky Strike segment (Escartín et al., 2014; Singh et al., 2006) and at the SWIR 50°28'E (Jian, Chen, et al., 2017; this study). The magmatically robust, ultraslow spreading endmember documented at the center of the SWIR 50°28'E segment is characterized by the highest proportion of lobate-sheet lava morphology among slow and ultraslow spreading ridges (Figure S6a), and by very low (<8%) apparent tectonic strain (Figure S6). Indeed, the apparent tectonic strain at the center of the SWIR 50°28'E segment and at the center of the Lucky Strike segment are similar to what has been observed at fast and intermediate spreading ridges (Figure S6b). Yet, the mid and lower crustal thermal and geological structure inferred for these slow and ultraslow ridge segment centers on the basis of seismic data differs from that of a fast-spreading ridge (Figure 9d). Melt supply, although in the highest range, fails to maintain a steady-state melt mush and shallow AML. The combination of a well-developed melt mush domain and a relatively long-lived AML that allows for a fast spreading-type mode of upper crustal construction (axial dome, localized dike injection, prevalence of high-effusion-rate lava, and very little faulting) is transient (with time scales of a few 100s kyr) and limited to a few kilometers at the very center of the most magmatically robust slow and ultraslow spreading segments.

## 5. Conclusions

We mapped the fine-scale volcanic and tectonic features at the center of the magmatically robust SWIR 50°28'E segment, and their evolution over the past 780 kyr, based on HR bathymetry and backscatter data, near-bottom magnetic data, and optical seafloor imagery. Our geological observations and interpretations support the following conclusions.

1. The study area displays three different volcanic seafloor morphologies, corresponding to different patterns of lava morphologies that are mainly influenced by lava effusion rates. High-effusion-rate, lobate-sheet lavas dominated, smooth and smooth hummocky morphologies are the most prevalent (64% of the mapped area), forming smooth domal volcanos, while low-effusion-rate, pillow lavas dominated, hummocky morphology accounts for only 29% (the remaining 7% is covered by sediments). The proportion of lobate-sheet lavas and the apparent tectonic strain are respectively 41% and <8%, similar to values measured at fast-spreading ridges.
2. We recognize six eruptive phases (V0–V5 from old to young), each corresponding to waxing or waning melt supply. Cycles that include a waxing and a waning phase last about 300 kyr. We propose that they result from temporal changes in the frequency of melt replenishment in the mid and lower crust. The most recent eruptions produce a ridge-parallel, fracture-free, hummocky domain that may have formed over the past ~19 kyr.
3. During waxing phases in magma supply, higher frequencies of melt replenishment keep the lower-crust hot, with relatively shallow, and long-lived AMLs and a melt-crystal mush zone. Narrow and localized dikes feed high-eruption-rate eruptions, forming smooth lava flows and domal volcanos that cover large



areas of the seafloor, with little to no faulting. Waxing phases at the SWIR 50°28'E segment represent the most magmatically robust endmember for ultraslow spreading ridges.

4. During waning phases in magma supply, lower frequencies of melt replenishment lead to deeper and shorter-lived AMLs, reduced melt-mush zones in the lower crust, a thicker brittle lithosphere, and a more variable and generally thicker hydrothermal domain. Crustal construction occurs within a wider zone of dike injection with more faults, producing dominantly hummocky lava flows.
5. The modes of upper-crustal construction and the magma plumbing systems at slow and ultraslow spreading ridges are controlled by spatial and temporal variations in magma supply more than by spreading rate alone.

## Data Availability Statement

Bathymetry and backscatter data used in this study are available at <https://doi.org/10.5281/zenodo.5147241>.

## References

- Appelgate, B., & Embley, R. W. (1992). Submarine tumuli and inflated tube-fed lava flows on Axial Volcano, Juan de Fuca Ridge. *Bulletin of Volcanology*, 54(6), 447–458. <https://doi.org/10.1007/BF00301391>
- Arnulf, A. F., Harding, A. J., Kent, G. M., & Wilcock, W. S. D. (2018). Structure, seismicity, and accretionary processes at the hot spot-influenced axial seamount on the Juan de Fuca Ridge. *Journal of Geophysical Research: Solid Earth*, 123(6), 4618–4646. <https://doi.org/10.1029/2017JB015131>
- Blacic, T. M., Ito, G., Canales, J. P., Detrick, R. S., & Sinton, J. (2004). Constructing the crust along the Galapagos Spreading Center 91.3°–95.5°W: Correlation of seismic layer 2A with axial magma lens and topographic characteristics. *Journal of Geophysical Research*, 109(B10). <https://doi.org/10.1029/2004JB003066>
- Cande, S. C., & Kent, D. V. (1995). Revised calibration of the geomagnetic polarity timescale for the Late Cretaceous and Cenozoic. *Journal of Geophysical Research*, 100(B4), 6093–6095. <https://doi.org/10.1029/94JB03098>
- Cann, J. R., & Smith, D. K. (2005). Evolution of volcanism and faulting in a segment of the Mid-Atlantic Ridge at 25°N. *Geochemistry, Geophysics, Geosystems*, 6(9), Q09008. <https://doi.org/10.1029/2005GC000954>
- Cannat, M., Rommevaux-Jestin, C., Sauter, D., Deplus, C., & Mendel, V. (1999). Formation of the axial relief at the very slow spreading Southwest Indian Ridge (49° to 69°E). *Journal of Geophysical Research*, 104(B10), 22825–22843. <https://doi.org/10.1029/1999JB900195>
- Cannat, M., Sauter, D., Lavier, L., Bickert, M., Momoh, E., & Leroy, S. (2019). On spreading modes and magma supply at slow and ultraslow mid-ocean ridges. *Earth and Planetary Science Letters*, 519, 223–233. <https://doi.org/10.1016/j.epsl.2019.05.012>
- Carbotte, S. M., Arnulf, A., Spiegelman, M., Lee, M., Harding, A., Kent, G., et al. (2020). Stacked sills forming a deep melt-mush feeder conduit beneath Axial Seamount. *Geology*, 48(7), 693–697. <https://doi.org/10.1130/g47223.1>
- Carbotte, S. M., Marjanović, M., Arnulf, A. F., Nedimović, M. R., Canales, J. P., & Arnoux, G. M. (2021). Stacked magma lenses beneath mid-ocean ridges: Insights from new seismic observations and synthesis with prior geophysical and geologic findings. *Journal of Geophysical Research: Solid Earth*, 126(4), e2020JB021434. <https://doi.org/10.1029/2020JB021434>
- Cashman, K. V., Sparks, R. S. J., & Blundy, J. D. (2017). Vertically extensive and unstable magmatic systems: A unified view of igneous processes. *Science*, 355(6331), eaag3055. <https://doi.org/10.1126/science.aag3055>
- Chen, Y., & Morgan, W. J. (1990). Rift valley/no rift valley transition at mid-ocean ridges. *Journal of Geophysical Research*, 95(B11), 17571–17581. <https://doi.org/10.1029/jb095ib11p17571>
- Clague, D. A., Paduan, J. B., Caress, D. W., Chadwick, Jr., W. W., Le Saout, M., Dreyer, B. M., et al. (2017). High-resolution AUV mapping and targeted ROV observations of three historical lava flows at Axial Seamount. *Oceanography*, 30(4), 82–99. <https://doi.org/10.5670/oceanog.2017.426>
- Colman, A., Sinton, J. M., White, S. M., McClintock, J. T., Bowles, J. A., Rubin, K. H., et al. (2012). Effects of variable magma supply on mid-ocean ridge eruptions: Constraints from mapped lava flow fields along the Galapagos Spreading Center. *Geochemistry, Geophysics, Geosystems*, 13(8), Q08014. <https://doi.org/10.1029/2012GC004163>
- Comber, V., Seher, T., Singh, S. C., Crawford, W. C., Cannat, M., Escartin, J., & Dusunur, D. (2015). Three-dimensional geometry of axial magma chamber roof and faults at Lucky Strike volcano on the Mid-Atlantic Ridge. *Journal of Geophysical Research: Solid Earth*, 120(8), 5379–5400. <https://doi.org/10.1002/2015JB012365>
- Cordier, C., Benoit, M., Hémond, C., Dyment, J., Le Gall, B., Briais, A., & Kitazawa, M. (2010). Time scales of melt extraction revealed by distribution of lava composition across a ridge axis. *Geochemistry, Geophysics, Geosystems*, 11(7), Q0AC06. <https://doi.org/10.1029/2010GC003074>
- Deschamps, A., Tivey, M., Embley, R. W., & Chadwick, W. W. (2007). Quantitative study of the deformation at Southern Explorer Ridge using high-resolution bathymetric data. *Earth and Planetary Science Letters*, 259(1–2), 1–17. <https://doi.org/10.1016/j.epsl.2007.04.007>
- Detrick, R. S., Buhl, P., Vera, E., Mutter, J., Orcutt, J., Madsen, J., & Brocher, T. (1987). Multi-channel seismic imaging of a crustal magma chamber along the East Pacific Rise. *Nature*, 326(6108), 35–41. <https://doi.org/10.1038/326035a0>
- Detrick, R. S., Mutter, J. C., Buhl, P., & Kim, I. I. (1990). No evidence from multichannel reflection data for a crustal magma chamber in the MARK area on the Mid-Atlantic Ridge. *Nature*, 347(6288), 61–64. <https://doi.org/10.1038/347061a0>
- Dunn, R. A., Toomey, D. R., & Solomon, S. C. (2000). Three-dimensional seismic structure and physical properties of the crust and shallow mantle beneath the East Pacific Rise at 9°30'N. *Journal of Geophysical Research*, 105(B10), 23537–23555. <https://doi.org/10.1029/2000JB900210>
- Escartin, J., Soule, S. A., Cannat, M., Fornari, D. J., Düşünür, D., & Garcia, R. (2014). Lucky Strike seamount: Implications for the emplacement and rifting of segment-centered volcanoes at slow spreading mid-ocean ridges. *Geochemistry, Geophysics, Geosystems*, 15(11), 4157–4179. <https://doi.org/10.1002/2014GC005477>
- Fan, Q., Olive, J. A., & Cannat, M. (2021). Thermo-mechanical state of ultraslow-spreading ridges with a transient magma supply. *Journal of Geophysical Research: Solid Earth*, 126(4), e2020JB020557. <https://doi.org/10.1029/2020JB020557>

## Acknowledgments

The authors thank the AUV QianLong II team of R/V XiangYangHong 10 and Tow-camera team of DaYangYi-Hao for collecting data. The authors are grateful to William Chadwick and an anonymous reviewer for their thorough reviews. Figures are generated using GMT-6 (Wessel et al., 2019). The AUV data collection and processing were supported by the National Key Research and Development Program of China (2018YFC0309901 and 2018YFC0309903) and by the COMRA Major Project (DY135-S1-01-01). J. Chen was supported by China Scholarship Council (201808330437) and ANR project “Ridge-Factory-Slow” (ANR-18-CE010002-01). This is IPGP contribution #4225.

- Fornari, D. J., Haymon, R. M., Perfit, M. R., Gregg, T. K. P., & Edwards, M. H. (1998). Axial summit trough of the East Pacific Rise 9°–10°N: Geological characteristics and evolution of the axial zone on fast spreading mid-ocean ridge. *Journal of Geophysical Research*, 103(B5), 9827–9855. <https://doi.org/10.1029/98JB00028>
- Fundis, A. T., Soule, S. A., Fornari, D. J., & Perfit, M. R. (2010). Paving the seafloor: Volcanic emplacement processes during the 2005–2006 eruptions at the fast spreading East Pacific Rise, 9°50′N. *Geochemistry, Geophysics, Geosystems*, 11(8), Q08024. <https://doi.org/10.1029/2010GC003058>
- Gregg, T. K. P., & Fink, J. H. (1995). Quantification of submarine lava-flow morphology through analog experiments. *Geology*, 23(1), 73–76. [https://doi.org/10.1130/0091-7613\(1995\)023<0073:QOSLFM>2.3.CO;2](https://doi.org/10.1130/0091-7613(1995)023<0073:QOSLFM>2.3.CO;2)
- Hooff, E. E. E., Detrick, R. S., Toomey, D. R., Collins, J. A., & Lin, J. (2000). Crustal thickness and structure along three contrasting spreading segments of the Mid-Atlantic Ridge, 33.5°–35°N. *Journal of Geophysical Research*, 105(B4), 8205–8226. <https://doi.org/10.1029/1999jb900442>
- Humphris, S. E., Fornari, D. J., Scheirer, D. S., German, C. R., & Parson, L. M. (2002). Geotectonic setting of hydrothermal activity on the summit of Lucky Strike Seamount (37°17′N, Mid-Atlantic Ridge). *Geochemistry, Geophysics, Geosystems*, 3(8), 1–25. <https://doi.org/10.1029/2001gc000284>
- Jian, H., Chen, Y. J., Singh, S. C., Li, J., Zhao, M., Ruan, A., & Qiu, X. (2017). Seismic structure and magmatic construction of crust at the ultraslow-spreading Southwest Indian Ridge at 50°28′E. *Journal of Geophysical Research: Solid Earth*, 122(1), 18–42. <https://doi.org/10.1002/2016JB013377>
- Jian, H., Singh, S. C., Chen, Y. J., & Li, J. (2017). Evidence of an axial magma chamber beneath the ultraslowspreading Southwest Indian Ridge. *Geology*, 45(2), 143–146. <https://doi.org/10.1130/G38356.1>
- Klischies, M., Petersen, S., & Devey, C. W. (2019). Geological mapping of the Menez Gwen segment at 37°50′N on the Mid-Atlantic Ridge: Implications for accretion mechanisms and associated hydrothermal activity at slow-spreading mid-ocean ridges. *Marine Geology*, 412, 107–122. <https://doi.org/10.1016/j.margeo.2019.03.012>
- Lin, J., Purdy, G. M., Schouten, H., Sempere, J.-C., & Zervas, C. (1990). Evidence from gravity data for focused magmatic accretion along the Mid-Atlantic Ridge. *Nature*, 344(6267), 627–632. <https://doi.org/10.1038/344627a0>
- Liu, X., Wang, S., Zhang, D., Cao, J., & Wang, H. (2016). Sounding data quality assessment method and result of high-resolution bathymetric sidescan sonar system. In *OCEANS 2016—Shanghai*. Institute of Electrical and Electronics Engineers Inc. <https://doi.org/10.1109/OCEANSAP.2016.7485446>
- Marjanović, M., Carbotte, S. M., Carton, H., Nedimović, M. R., Mutter, J. C., & Canales, J. P. (2014). A multi-sill magma plumbing system beneath the axis of the East Pacific Rise. *Nature Geoscience*, 7(11), 825–829. <https://doi.org/10.1038/ngeo2272>
- Mendel, V., Sauter, D., Rommevaux-Jestin, C., Patriat, P., Lefebvre, F., & Parson, L. M. (2003). Magmato-tectonic cyclicity at the ultra-slow spreading Southwest Indian Ridge: Evidence from variations of axial volcanic ridge morphology and abyssal hills pattern. *Geochemistry, Geophysics, Geosystems*, 4(5), 9102. <https://doi.org/10.1029/2002GC000417>
- Minschull, T. A., Muller, M. R., & White, R. S. (2006). Crustal structure of the Southwest Indian Ridge at 66°E: Seismic constraints. *Geophysical Journal International*, 166(1), 135–147. <https://doi.org/10.1111/j.1365-246X.2006.03001.x>
- Morgan, J. P., & Chen, Y. J. (1993). The genesis of oceanic crust: Magma injection, hydrothermal circulation, and crustal flow. *Journal of Geophysical Research*, 98(B4), 6283–6297. <https://doi.org/10.1029/92jb02650>
- Panagiotakis, C., & Kokinou, E. (2015). Linear pattern detection of geological faults via a topology and shape optimization method. *IEEE Journal of Selected Topics in Applied Earth Observations and Remote Sensing*, 8(1), 3–11. <https://doi.org/10.1109/JSTARS.2014.2363080>
- Patriat, P., Sloan, H., & Sauter, D. (2008). From slow to ultraslow: A previously undetected event at the Southwest Indian Ridge at ca. 24 Ma. *Geology*, 36(3), 207–210. <https://doi.org/10.1130/G24270A.1>
- Perfit, M. R., & Chadwick, W. W. (1998). Magmatism at mid-ocean ridges: Constraints from volcanological and geochemical investigations. *Geophysical Monograph Series*, 106, 59–115. <https://doi.org/10.1029/GM106p0059>
- Rabinowicz, M., & Toplis, M. J. (2009). Melt segregation in the lower part of the partially molten mantle zone beneath an oceanic spreading centre: Numerical modelling of the combined effects of shear segregation and compaction. *Journal of Petrology*, 50(6), 1071–1106. <https://doi.org/10.1093/ptrology/egp033>
- Rioux, M., Cheadle, M. J., John, B. E., & Bowring, S. A. (2016). The temporal and spatial distribution of magmatism during lower crustal accretion at an ultraslow-spreading ridge: High-precision U-Pb zircon dating of ODP Holes 735B and 1105A, Atlantis Bank, Southwest Indian Ridge. *Earth and Planetary Science Letters*, 449, 395–406. <https://doi.org/10.1016/j.epsl.2016.05.047>
- Rubin, A. M., & Pollard, D. D. (1988). Dike-induced faulting in rift zones of Iceland and Afar. *Geology*, 16(5), 413–417. [https://doi.org/10.1130/0091-7613\(1988\)016<0413:DIFIRZ>2.3.CO;2](https://doi.org/10.1130/0091-7613(1988)016<0413:DIFIRZ>2.3.CO;2)
- Sauter, D., Cannat, M., Meyzen, C., Bezos, A., Patriat, P., Humler, E., & Debayle, E. (2009). Propagation of a melting anomaly along the ultraslow Southwest Indian Ridge between 46°E and 52°20′E: Interaction with the Crozet hotspot? *Geophysical Journal International*, 179(2), 687–699. <https://doi.org/10.1111/j.1365-246X.2009.04308.x>
- Sauter, D., Parson, L., Mendel, V., Rommevaux-Jestin, C., Gomez, O., Briais, A., et al. (2002). TOBI sidescan sonar imagery of the very slow-spreading Southwest Indian Ridge: Evidence for along-axis magma distribution. *Earth and Planetary Science Letters*, 199(1–2), 81–95. [https://doi.org/10.1016/S0012-821X\(02\)00543-5](https://doi.org/10.1016/S0012-821X(02)00543-5)
- Searle, R. C., Murton, B. J., Achenbach, K., LeBas, T., Tivey, M., Yeo, I., et al. (2010). Structure and development of an axial volcanic ridge: Mid-Atlantic Ridge, 45°N. *Earth and Planetary Science Letters*, 299(1–2), 228–241. <https://doi.org/10.1016/j.epsl.2010.09.003>
- Seher, T., Crawford, W. C., Singh, S. C., Cannat, M., Combier, V., & Dusunur, D. (2010). Crustal velocity structure of the Lucky Strike segment of the Mid-Atlantic Ridge at 37°N from seismic refraction measurements. *Journal of Geophysical Research*, 115(3), B03103. <https://doi.org/10.1029/2009JB006650>
- Singh, S. C., Crawford, W. C., Carton, H., Seher, T., Combier, V., Cannat, M., et al. (2006). Discovery of a magma chamber and faults beneath a Mid-Atlantic Ridge hydrothermal field. *Nature*, 442(7106), 1029–1032. <https://doi.org/10.1038/nature05105>
- Tao, C., Lin, J., Guo, S., Chen, Y. J., Wu, G., Han, X., et al. (2012). First active hydrothermal vents on an ultraslow-spreading center: Southwest Indian Ridge. *Geology*, 40(1), 47–50. <https://doi.org/10.1130/G32389.1>
- Thébault, E., Finlay, C. C., Beggan, C. D., Alken, P., Aubert, J., Barrois, O., et al. (2015). International geomagnetic reference field: The 12th generation international geomagnetic reference field—The twelfth generation. *Earth Planets and Space*, 67(1), 79. <https://doi.org/10.1186/s40623-015-0228-9>
- Wessel, P., Luis, J. F., Uieda, L., Scharroo, R., Wobbe, F., Smith, W. H. F., & Tian, D. (2019). The generic mapping tools version 6. *Geochemistry, Geophysics, Geosystems*, 20(11), 5556–5564. <https://doi.org/10.1029/2019GC008515>
- Wu, T., Tao, C., Zhang, J., Wang, A., Zhang, G., Zhou, J., & Deng, X. (2019). A hydrothermal investigation system for the Qianlong-II autonomous underwater vehicle. *Acta Oceanologica Sinica*, 38(3), 159–165. <https://doi.org/10.1007/s13131-019-1408-4>

- Yu, Z., Li, J., Niu, X., Rawlinson, N., Ruan, A., Wang, W., et al. (2018). Lithospheric structure and tectonic processes constrained by microearthquake activity at the central ultraslow-spreading Southwest Indian Ridge (49.2° to 50.8°E). *Journal of Geophysical Research: Solid Earth*, *123*(8), 6247–6262. <https://doi.org/10.1029/2017JB015367>
- Yue, X., Li, H., Ren, J., Tao, C., Zhou, J., Wang, Y., & Lü, X. (2019). Seafloor hydrothermal activity along mid-ocean ridge with strong melt supply: Study from segment 27, southwest Indian ridge. *Scientific Reports*, *9*(1), 9874. <https://doi.org/10.1038/s41598-019-46299-1>